1   **Uppermost mantle velocity beneath the Mid-Atlantic Ridge and transform**

2   **faults in the Equatorial Atlantic Ocean**

3   Guilherme W. S. de Melo, Ross Parnell-Turner, Robert P. Dziak, Deborah K. Smith,

4   Marcia Maia, Aderson F. do Nascimento, and Jean-Yves Royer

5

6   **Abstract**

7   Seismic rays that travel just below the Moho discontinuity provide useful insights into the thermal

8   and compositional properties of the upper-mantle, and can be detected as *Pn* phases from regional

9   earthquakes. Such phases are routinely identified in the continents. In the oceans, however,

10   detection of *Pn* phases is limited due to the lack of long-term instrument deployments. Here, we

11   present estimates of upper-mantle velocity in the Equatorial Atlantic Ocean from *Pn* arrivals

12   beneath, and flanking, the Mid-Atlantic Ridge, and across several transform faults. We analyzed

13   waveforms from 50 regional earthquakes with magnitude $M_W > 3.5$ recorded over 12 months in

14   2012–2013 by five autonomous hydrophones and a single broadband seismic station located on

15   the St. Peter and St. Paul archipelago. The resulting catalog of 152 ray paths allows us to resolve

16   spatial variations in upper-mantle velocities, which are consistent with estimates from nearby

17   wide-angle seismic experiments. We find relatively fast upper-mantle velocities near to the St.

18   Paul transform system ($\sim$8.4 km s^{-1}), compared to slower velocities parallel to the ridge axis ($\sim$7.7

19   km s^{-1}). Hence, this method is able to resolve ridge-transform scale velocity variations. Ray paths

20   in lithosphere younger than 10 Myr show velocities with mean of 7.9 ± 0.5 km s^{-1}, which is slightly

21   slower than those sampling lithosphere older than 20 Myr (8.1 km ± 0.3 s^{-1}). There is no apparent

22   systematic relationship between velocity and ray azimuth, nor any correlation between upper-

23   mantle *Pn* velocity and shear wave speeds from the global SL2013sv model at depths < 150 km.

24   Our results demonstrate that data from long-term deployments of autonomous hydrophones can

25   be used to obtain rare and insightful estimates of uppermost mantle velocities over hundreds of

26   kilometers, in otherwise inaccessible parts of the deep oceans.

27

28   **Introduction**

29   Seismic velocity measurements provide a useful proxy for investigating spatial variations in upper-

30   mantle properties, such as temperature and anisotropy, with implications for melt supply and

31   mantle heterogeneity (e.g. Lin and Phipps Morgan, 1992; Dunn *et al.*, 2005). These measurements

32   are relatively straightforward to obtain on the continents (e.g. Chulick and Mooney, 2002; Chulick

33   *et al.*, 2013). However, it remains challenging and expensive to measure upper-mantle seismic

34   velocity in the deep ocean basins, due to their remote location and challenges of deploying long-

35   term instruments on the seafloor. *Pn* phases are critically refracted rays that are guided through

36   an interface in the lithospheric mantle (Linehan, 1940; Brandsdottir and Menke, 1997), and can

37   be recorded by seafloor-moored hydrophones, which in turn can be used to estimate upper-mantle

38   seismic velocity (Walker *et al.*, 1983; Slack *et al.*, 1999). At the Mid-Atlantic Ridge (MAR) from

39   10°N to 35°N, *Pn* arrivals from 48 individual ray paths were identified using hydrophone-recorded

40   data and used to investigate upper-mantle velocities, giving a mean velocity of 8.0 ± 0.1 km s^{-1}

41   (Dziak *et al.*, 2004). This velocity estimate was higher than that from nearby active source seismic

42   experiments along the ridge axis (7.5–7.9 km s^{-1}; Canales *et al.*, 2000), probably due to the effects

43   of younger and thinner oceanic lithosphere being sampled by the refraction profiles, and the effects

44   of averaging velocities across all rays. Despite these advances, upper-mantle velocities across

45   deep ocean basins remain poorly constrained, and the potential for *Pn* travel times from

46   hydrophone-recorded data to resolve spatial variations in upper-mantle velocity has not yet been

47 sufficiently tested.

48   Here, we use *Pn* arrivals from regional earthquakes to constrain upper-mantle velocity in

49 the remote Equatorial Atlantic Ocean. Arrivals were recorded by a combination of five moored

50 hydrophones and a single seismograph station installed on the St. Peter and St. Paul islets, giving

51 a total of 152 ray paths that sample mantle conditions both on- and off-axis, and across the St Paul

52 transform system. Our study is coincident with several mantle velocity estimates from a wide-

53 angle seismic experiment (Le Pichon *et al.*, 1965), and hence has the opportunity to validate spatial

54 variations in velocity revealed by groups of similar ray paths.

55

56 ***Equatorial Atlantic Ocean***

57   In our study region of the Equatorial Atlantic Ocean (10ºN–5ºS and 34W-21W), the MAR

58 is offset by some of the longest transform faults on Earth, including the Strakhov, St Paul, and

59 Romanche transforms (Figure 1). The St Paul transform system consists of four transform faults

60 and three intra-transform ridge segments that accommodate an offset of 630 km. The northwest

61 transform fault is currently undergoing transpression, giving rise to the ~200 km-long and ~30 km-

62 wide Atobá ridge (Maia *et al.*, 2016), and also uplift of 1.5mm yr^{-1} at the St Peter and St Paul islets

63 (Campos *et al.*, 2010; Maia *et al.*, 2016). Other transforms in the system do not host topographic

64 highs or an island related to transpression, and hence presumably are not experiencing uplift. In

65 the three intervening spreading segments, seafloor spreading is slow, at ~20 mm yr^{-1} average half

66 rate (DeMets *et al.*, 2010). Faulting plays an important role in crustal accretion, and seismicity

67 rates are relatively high, providing a useful tool to investigate the properties of the crust and upper

68 mantle, as well as deformation at long-offset strike-slip systems (e.g. Francis *et al.*, 1978;

69 Abercrombie and Ekstrom, 2001; de Melo and do Nascimento, 2018).

70

71   **Methods**

72   ***Hydroacoustic Waves***

73   Hydrophones moored in the Sound Fixing and Ranging (SOFAR) channel routinely record

74   T-phases, and also acoustic-converted *P*-waves from regional and teleseismic earthquakes (e.g.

75   Dziak *et al.*, 1997, 2004; Slack *et al.*, 1999; Sohn and Hildebrand, 2001). Seismic waves from

76   regional earthquakes are expected to propagate along the Moho discontinuity as *Pn* phases, and

77   convert to an acoustic phase on the seafloor near to the hydrophone mooring, where they can be

78   detected (e.g. Dziak *et al.*, 2004). Identification of acoustic-converted *Pn* phases on moored

79   autonomous hydrophone records provides a simple and effective method to estimate upper-mantle

80   velocities in remote locations. Compared to long-term broadband ocean bottom seismograph

81   deployments, or wide-angle active source seismic experiments, arrays of these moored instruments

82   are relatively inexpensive to build (e.g. Fox *et al.*, 2001).

83

84   ***Waveform Data***

85   We analyzed *Pn* arrivals in waveform data recorded by a combination of five moored

86   autonomous hydrophones and one land-based seismograph (Figure 2). The five autonomous

87   hydrophone instruments were deployed during two separate experiments: stations EA2 and EA8

88   were part of the Equatorial Atlantic (EA) array (Smith et al., 2012). Data were recorded at 16-bit

89   resolution and a sampling rate of 250 Hz; for further details on these hydrophone instruments see

90   Fox *et al.* (2001). Hydrophones H2, H4, H5 were deployed during the COLd Mantle Exhumation

91   and Intra-transform Accretion experiment (COLMEIA; Maia *et al.*, 2014, 2016), and recorded

92   data at 24 bit-resolution with a sampling rate of 240 Hz; for further instrument details see D'Eu

93   *et al.*(2012). We also used waveform data recorded by a three-component broadband

94   seismograph installed at the Saint Peter and Saint Paul Archipelago Scientific Station on the

95   Belmonte islet (ASPSP; de Melo and do Nascimento, 2018). This station is operated by the

96   Seismological Laboratory of Federal University of Rio Grande do Norte in cooperation with the

97   Brazilian Navy. The sparse distribution and mixed instrument types we used means that data

98   coverage is uneven, as shown in Figure 1b. Waveform data were examined for the time period

99   from July 2012 to July 2013, using a combination of the five hydrophones and the ASPSP

100   seismograph, with recording intervals dictated by technical challenges and vessel schedules.

101   Prior to manually picking *Pn* arrivals, we applied a 6–20 Hz Butterworth bandpass filter to

102   the hydrophone data in order to suppress unwanted noise. A bandpass filter with range 4–12 Hz

103   was applied prior to picking arrivals from the ASPSP seismograph, to suppress additional

104   microseism noise due to its island location.

105

106   ***Pn analysis***

107   We used regional *P*-wave arrivals recorded by the five autonomous hydrophones and by

108   the ASPSP seismograph to identify *Pn* phases that have travelled within the uppermost mantle in

109   the Equatorial Atlantic Ocean. During the 12 month-long observation period, *P*-wave arrivals

110   from 50 regional earthquakes were recorded. Based upon origin time, events were manually

111   associated with earthquakes in the International Seismological Center Bulletin (ISC;

112   www.isc.ac.uk), yielding hypocenter locations, origin times, and magnitudes ranging from 3.5 to

113   5.4 M$_W$. Earthquakes dominantly arise due to strike-slip faulting along the Strakhov, St. Paul, and

114   Romanche transform faults, with additional events due to extension along the intervening

115   spreading ridge segments (Figure 2a). Three example arrivals from these events are shown in

116   Figures 3 and 4, highlighting the typical response to strike-slip and normal faulting earthquakes,

117   which range in magnitude from 4.6 to 5.3 M$_W$. Typical *P*-arrivals have sufficient signal-to-noise

118   ratio for picking (noted in Figures 3 and 4), and linear move-out, consistent with upper mantle

119   velocity, is evident across the hydrophone array stations due to wave propagation along the crust-

120   mantle interface (see common-receiver plots in Supplementary Figures S1–S6). *P*-arrivals are

121   easily distinguished from *T*-phase arrivals, which arrive much later than *P*-arrivals, are emergent

122   in character, and are higher in amplitude than *P*-arrivals (see hydrophone H5 in Figure 4). The

123   catalog of detected events is given in Table S1.

124   In order to further test whether the detected arrivals were *Pn* phases, we compared the observed

125   travel times to those predicted by the global IASP91 velocity model (Kennett and Engdahl, 1991).

126   For each source-receiver ray path, we calculated the predicted *Pn* arrival time using IASP91, with

127   the addition of a station-dependent delay to account for the propagation time from seafloor to

128   hydrophone. This delay (1.2–2.5 s) was estimated using the hydrophone mooring cable length at

129   each station, and the local water sound velocity estimated from the Global Ocean Sound Speed

130   Profile Library (Barlow, 2019), values are given in Table 1. The predicted *Pn* arrival times differ

131   from the observed *Pn* arrivals by 5–10 s (Figures 3 and 4), however this is not surprising since the

132   IASP91 model contains a crustal layer that is much thicker (30 km) than that expected in the oceans

133   (~6 km). Hence, the differences in observed and predicted *Pn* arrival time are probably dominated

134   by this additional crustal layer thickness in the velocity model, plus earthquake location and origin

135   time uncertainties. Although these differences are evident, the waveform character and linear

136   move-out velocity means that we are confident in our identification of these high signal-to-noise

137   phases as *Pn* arrivals.

138   ISC origin times were subtracted from the *Pn* arrival times to obtain travel times for each

139   ray path (i.e. each event-station pair), and the *Pn* velocity estimated by dividing this travel time by

140   the great-circle (i.e. shortest) epicentral distance from event to station. We account for oceanic

141   crust by subtracting ray path distances and travel times for the portion of the path that travels

142   through the crust, assuming that all events occurred at 10 km depth (ISC catalog), and that crustal

143   thickness is uniformly 6 km (Christeson *et al.*, 2019). For each station, we then calculate the

144   distance and travel time for the portion of the ray path that extends from an earthquake in the crust

145   to the Moho, and back from the Moho through the entire oceanic crustal thickness. Details of these

146   corrections for each station are given in Table 1.

147   Our approach yielded a total of 152 ray paths and hence 152 separate *Pn* velocity estimates

148   from the catalog of 50 regional earthquakes (Figure 5). Although epicentral distance ranges greatly

149   from 32 km to ~1095 km, all 50 events were detected at all available stations, implying that the

150   detection threshold of the combined hydrophones and ASPSP station is at least as low as M_W 3.5.

151   Since most stations were located either near to, or to the north of, the St Paul fracture zone, our

152   ray path coverage is more comprehensive in the northern part of the study area. Ray paths

153   sampling upper-mantle velocities to the south of the St Paul fracture zone are restricted to events

154   detected by hydrophone EA8, and those originating from four earthquakes located at the eastern

155   end of the Romanche transform fault (Figure 5).

156

157   ***Pn velocity uncertainty***

158   The two most significant potential sources of error are in the hypocenter locations of events

159   in the ISC Catalog, and in the *Pn* arrival picks. These two sources of error directly influence ray

160   path length and travel time, respectively. We estimated hypocenter location (and hence epicentral

161   distance) error to be ± 10 km, based upon ISC catalogue location uncertainty, and typical error in

162   global earthquake location (Lohman and Simons, 2005; Weston *et al.*, 2012). Arrival pick (and

163   hence also travel time) errors were estimated based upon qualitative station-dependent pick

164   uncertainties, defined as ± 0.5 s for EA2 and EA8; ± 1.0 s for H2, H4 and H5; and ± 0.3 s for

165   ASPSP. The total uncertainty in our velocity estimate, δv, was estimated by formally propagating

166   the errors in epicentral distance, *d*, and travel time, *t*, as follows

167

$$\delta v = v \sqrt{\left(\frac{\delta d}{d}\right)^2 + \left(\frac{\delta t}{t}\right)^2},$$

168   where the *d* and *δd* are epicentral distance and its respective error, and *t and δt* are travel time and

169   its respective error (e.g. Taylor, 1997).

170   Although receiver location uncertainty is negligible for the land station ASPSP (located via

171   the Global Positioning System), there is potential location uncertainty for the moored hydrophones

172   in our network. Moored hydrophone locations were obtained by acoustic triangulation between

173   the mooring acoustic release and the deployment vessel soon after the moorings settled on the

174   seafloor, within error of several meters. In order to account for the possibility of abnormally strong

175   current motion, each instrument is fitted with a pressure and temperature logger below the

176   floatation package, so that any significant hydrophone depth changes would be recorded (e.g. Fox

177   *et al.*, 2001). Significant depth changes were not detected during our experiment, and thus we

178   assume that the hydrophone location was constant during data collection, and hence uncertainty is

179   relatively minor.

180   **Results**

181   *Pn velocities*

182   The catalog of 152 *Pn* ray paths (Figure 5b) and travel times (Figure 6) indicates upper-

183   mantle velocities that vary considerably across the study area, with estimates ranging between 7.2

184   and 11.1 km s^{-1}, with uncertainties ranging from 0.1 to 1.9 km s^{-1} (Table S2). At the center of the

185   study area there appears to be a longitudinal variation in *Pn* velocity, with events originating near

186   the St Paul transform system, and sampling adjacent lithosphere, having higher velocities than

187   those from the adjacent spreading centers (Figure 5a).   The best constrained estimate for sub-axis,

188   ridge-parallel mantle velocity comes from ray paths that sample the portion of the spreading axis

189   between the Strakhov fracture zone and stations near the St Paul fracture zone (H2, H5 and ASPSP).

190   Here, *Pn* travel times consistently imply relatively slow velocities, with a mean of 7.7 km s^{-1}.

191   Slightly faster velocities ranging between 7.8 and 8.2 km s^{-1} are indicated by ray paths between

192   hydrophone EA2 and the Strakhov fracture zone, oriented roughly parallel to a plate spreading

193   flowline.   Ray paths oriented southwest-northeast (azimuth ~060°), i.e. oblique to the spreading

194   direction, between events on the St Paul fracture zone and detected at hydrophone EA2, have some

195   of the fastest mantle velocities (between 7.6 and 8.5 km s^{-1}) compared to other rays sampling areas

196   unaffected by fracture zones. Velocity estimates in the vicinity of the St Paul fracture zone itself

197   (from transform faulting events detected by hydrophones H2, H4 and H5, and ASPSP) show

198   considerable variation, ranging from 8.0 to 9.1 km s^{-1} and a mean of 8.4 km s^{-1}, and little apparent

199   spatial consistency. Among these events, we encountered one of the fastest *Pn* velocities (9.0 km

200   ± 0.2 s^{-1}) in this study, for a ray path oriented roughly parallel to the St Paul transform fault (ray

201   azimuth ~105°) between an event near the St Paul islets and detected by hydrophone H4.

202   South of the St Paul fracture zone, ray paths from events detected by hydrophone EA8

203   showed considerable variation in upper-mantle velocity, which range from 7.2 to 9.0 km s^{-1}. Ray

204   paths originating from the spreading axis north of the St Paul transform fault and trending ~170°

205   towards EA8, have velocities of 7.3–8.1 km s^{-1}, while ray paths from the St Paul transform fault

206   trending ~185° towards EA8 have consistently faster velocities of 7.6–9.1 km s^{-1}.

207   Only 12 ray paths sampling the upper-mantle parallel and adjacent to the spreading axis

208   between the southern extent of the St Paul transform fault and the Romanche transform fault are

209   available. This relatively poor coverage in ray paths in this area hinders our interpretation, where

210   velocities range from 7.2 to 8.3 km s^{-1}.

211

212   **Discussion**

213   ***Upper-mantle velocity structure***

214   In general, rays originating from the St Paul transform system are faster than those

215   originating from active spreading centers to the east and west (Figure 5a), probably due to cooler

216   conditions at the Moho along the transform, giving higher velocities. Our estimates of upper-

217   mantle *Pn* velocities broadly agree (within error) with *Pn* velocities from radially stratified velocity

218   models such as PREM (Dziewonski and Anderson, 1981) and IASP91 (Figure 6; Kennett and

219   Engdahl, 1991). *Pn* velocity estimates from this study are also consistent with mantle velocity

220   estimates from a series of reversed wide-angle refraction seismic profiles (i.e. with multiple shot

221   points giving overlapping coverage) collected in the equatorial Atlantic during R/V *Atlantis* cruise

222   A180 (Figure 5b; Le Pichon *et al.,* 1965). The modal difference in velocity between refraction

223   profiles from Le Pichon *et al.* (1965) and all intersecting ray paths is 0.2 km s^{-1} (see histogram in

224   Figure 5c), although our *Pn* velocity estimates are typically slower than those reported by Le

225   Pichon *et al.* (1965), with a maximum disagreement of 1.2 km s^{-1}. A mantle velocity of 8.30 km

226   s^{-1} was reported along profile A180-48, which is 283 km-long, and crosses the eastern side of the

227   St Paul transform fault (near ~26.3°W), trending northeast-southwest (Figure 5b). This velocity

228   is consistent with that inferred from *Pn* ray paths with a similar orientation, originating from

229   earthquakes on the St Paul transform fault that were detected by hydrophone EA8.   Ray paths that

230   intersect profile A180-48 (at angles either perpendicular or oblique to the trend of the refraction

231   profile) typically indicate slower upper-mantle velocities, ranging from 7.3 to 8.1 km s^{-1}, with the

232   exception of one anomalous ray path oriented parallel with the St Paul transform fault with a

233   velocity of 9.0 km s^{-1}. Refraction profiles A180-40 and -42 are oriented roughly east-west, are

234   located ~100 km north of the Romanche transform fault, and have velocities of 8.03 and 8.49 km

235   s^{-1}, respectively. Although there are only four *Pn* ray paths near to these profiles, with near-

236   perpendicular orientation, they indicate velocities ranging from 7.6 to 8.2 km s^{-1}, and hence are in

237   broad agreement.   Our results are also in close agreement with a velocity estimate of 8 km s^{-1}

238   from an active source experiment near 18°W roughly perpendicular to the St Paul fracture zone,

239   which at this longitude separates 40 Myr old crust in the south from 70 Myr old crust in the north

240   (Growe *et al.*, 2019). The generally good agreement between upper-mantle velocities from the

241   refraction profiles and our *Pn* arrivals validates our results, and implies that spatial trends observed

242   in the study area are likely to be real.

243   Elsewhere along the MAR, between 10º to 40ºN, a mean upper-mantle velocity of 8.0 km

244   ± 0.1 km s^{-1} was estimated using a similar method to this study with *Pn* arrivals detected by an

245   array of autonomous hydrophones (Dziak *et al.,* 2004). In common with this study, ray paths used

246   by Dziak *et al.,* (2004) often crossed the ridge axis, spanned a series of fracture zones, and extended

247   onto older crust, which may explain the close agreement in results. This result suggests that off-

248   axis and on-axis upper mantle characteristics are similar in the north and equatorial Atlantic Ocean.

249   Near the Oceanographer transform fault (~35°N), two-dimensional tomographic inversion

250   of wide-angle seismic refraction data located along the ridge axis suggest velocities of 7.4–7.8 km

251   s^{-1} (Canales *et al.*, 2000; Hooft *et al.*, 2000). These results agree closely with our estimates of *Pn*

252   velocity from rays sampling on-axis upper-mantle to the north of the St Paul transform fault

253   (Figure 5b).

254

255   ***Upper-mantle velocity and plate age***

256   Due to upwelling of hot material, seismic velocities in the upper-mantle near to the ridge

257   axis are expected to be lower than in off-axis areas (e.g. Turcotte and Schubert, 2002). Following

258   the removal of minor gridding artifacts associated with fracture zone traces, we used the global

259   crustal age model (Müller et al., 2008) to assign a mean age along each ray path, for comparison

260   with *Pn* velocity (Figure 7a).

261   Ray paths along lithosphere younger than 10 Ma show a wide range of velocities, with a

262   mean of 7.9 km s^{-1} and standard deviation of 0.5 km s^{-1}. Twenty of the ray paths yield velocities

263   less than 7.5 km s^{-1}. *Pn* velocities for ray paths along lithosphere older than 20 Ma are typically

264   slightly faster, with a mean of 8.1 km s^{-1} and standard deviation of 0.3 km s^{-1}, while only two

265   estimates give velocities slower than 7.5 km s^{-1} (Figure 7a). Most rays cover a wide range of crustal

266   ages, so this geometry, and our averaging approach, may smear the possible effects of lithospheric

267   ageing.   The lack of rays travelling exclusively via older lithosphere may also obscure any

268   progressive trend between upper-mantle velocity and crustal age. However, the tendency toward

269   the inclusion of slower velocities in younger crust (Figure 7) reflects the expected variation with

270   respect to the zone of axial upwelling.

271

272   ***Azimuthal Seismic Anisotropy***

273   Laboratory experiments have shown that the mantle can experience significant shear strain

274   during corner flow at the ridge axis, leaving an anisotropic fabric in the lithospheric mantle as

275   minerals (e.g. olivine) are aligned into a lattice preferred orientation (LPO; e.g. Zhang and Karato,

276   1995; Nicolas and Christensen, 2011). Anisotropy consistent with a LPO formed by two-

277   dimensional mantle flow has been measured at some locations in the oceanic upper mantle (e.g.

278   Raitt *et al.*, 1969; Lin *et al.*, 2016), however the strength of anisotropy varies widely, and debate

279   remains about its origins (e.g. Mark *et al.*, 2019). Since isochrons in this region are fairly uniform

280   (Figure 7), V_{Pn} anisotropy could be expected parallel to paleo-relative plate motion, although this

281   assumption has been shown to not apply everywhere (VanderBeek and Toomey, 2017).

282   We investigated the dependence of mantle velocity with azimuth, and use epicentral

283   distance as a proxy for depth of mantle penetration to group rays (Figure 7b). No discernable

284   pattern is evident in rays grouped by epicentral distance, including those expected to sample

285   deepest in the mantle with epicentral distances > 700 km (blue lines in Figure 7c). Removing rays

286   with V_{Pn} error > 0.4 km s^{-1} also does not resolve any azimuthal dependence (Figure 7d), nor does

287   separating rays by mean crustal age (Figures 7e and 7f).

288   The apparent lack of such azimuthal dependence could be due to several reasons. First,

289   azimuthal dependence may be too subtle to be resolved by our V_{Pn} estimates, given the

290   uncertainties in hypocenter location and crustal thickness discussed above. Second, the slow

291   spreading rate of the MAR (≈22 mm/yr total rate) may result in a thickened lithosphere that is

292   dominantly cooled by conduction, thus inhibiting corner flow (e.g. Sleep, 1975). As a result,

293   deformation could be accommodated by faulting at depths of 5–10 km beneath the Moho, reducing

294   the viscous strain in the mantle at these depths, and suppressing the anisotropy recorded in the

295   mantle (e.g. Ribe, 1989). Observations of weaker or anomalous anisotropy elsewhere in the

296   Atlantic Ocean are consistent with our findings (e.g. Gaherty *et al.*, 2004; Dunn *et al.*, 2005). Third,

297   complex, three-dimensional upwelling patterns near the ridge axis could result in anisotropy on

298   relatively short wavelengths (Lin and Phipps Morgan, 1992), which would be smeared along our

299   relatively long ray paths, and hence not be resolved.

300

301   ***Pn and surface wave velocity***

302   To explore the relationship between V_{Pn} and the thermal structure of the asthenospheric

303   upper-mantle, we compared our velocity estimates with a global, vertically polarized shear speed

304   model SL2013sv (Schaeffer and Lebedev, 2013). Our objective is to consider our observations

305   of uppermost mantle properties in the context of deeper mantle anomalies. We do not aim to

306   validate our V_{Pn} estimates via this comparison. This model was chosen because it is particularly

307   sensitive to anomalies within the upper-mantle, and hence provides a window into the upper mantle

308   structure directly beneath our *Pn* ray paths. We extracted values of vertically polarized

309   tomographic shear velocity anomaly (*%dVs*) at 100 km intervals along each ray path from slices

310   through the SL2013sv model at depths of 25, 50, 75 and 150 km. We then calculated the

311   mean *%dVs* along each ray path, at each depth interval (Figure 8). At 25 and 50 km depths, the

312   effects of the ridge axis are evident, with faster velocities associated with ray paths travelling off-

313   axis (detected by EA2 and EA8), and hence not sampling the relatively slow axial region (Figures

314   8a and 8b). This effect is less pronounced at 75 km depth (Figure 8c), and is not apparent at 150

315   km depth, which presumably reflects sub-plate velocities. The lack of correlation between

316   SL2013sv and *Pn* velocities at 150 km suggests that our V_{Pn} estimates, sensitive to the velocity

317   structure directly beneath the Moho, do not record deeper, larger-scale sub-plate (i.e.

318   asthenospheric) processes and anomalies. Hence our observed V_{Pn} variability may instead arise

319   due to local variations in melt supply, lithospheric thickness, or faulting.

320

321   **Conclusions**

322   We used a network of five autonomous hydrophones combined with a single island

323   seismograph to detect *Pn* arrivals from regional earthquakes in the Equatorial Atlantic Ocean over

324   a period of ~12 months between 2012 and 2013. We estimated upper-mantle velocities using the

325   travel times of 152 *Pn* arrivals, and find that our estimates are in good agreement with independent

326   estimates of upper-mantle velocities from nearby seismic refraction experiments.

327   We find that the upper-mantle near the St Paul transform system has consistently fast

328   velocities (>8 km s^{-1}), compared to relatively slow velocities (~7.5 km s^{-1}) in the adjacent Mid-

329   Atlantic Ridge spreading segments northwest of the transform. This spatial pattern is consistent

330   with the notion that *Pn* ray paths sample slower velocities in areas of crustal accretion near the

331   ridge axis, and faster velocities in areas of transforms which are in general, cooler, despite the

332   presence of intra-transform spreading segments. We do not resolve any dependence between V_{Pn}

333   and azimuth, which could either be due to observational uncertainty, or, due to the combined effects

334   of thickened lithosphere and more complex mantle upwelling patterns. We also do not find any

335   correlation between V_{Pn} velocities and vertically polarized shear speed from the global SL2013sv

336   model, indicating that our method is not sensitive to properties of the asthenosphere. The good

337   agreement between our results and those from seismic refraction experiments demonstrates that

338   the relatively simple method of using sparse arrays of autonomous hydrophones to detect *Pn*

339   arrivals can be used to obtain accurate estimates of upper-mantle velocities. Hence, this method

340 provides a useful complement to deployments of other seafloor instruments such as ocean bottom

341 seismographs, in remote areas where direct observations are typically elusive.

342

343 **Acknowledgements**

357

358 **References**

359 Abercrombie, R. E., and G. Ekstrom (2001). Earthquake slip on oceanic transform faults, *Nature*

360 **410**, 74–77.

361 Barlow, J. (2019). Global Ocean Sound Speed Profile Library (GOSSPL), an Rdata resource for

362 studies of ocean sound propagation, *NOAA Tech. Memo. NMFS SWFSC* **612**, no. March, 1–

363   7, doi: 10.25923/7DJ1-J540.

364 Brandsdottir, B., and W. Menke (1997). Faroe-Iceland Ridge Experiment, 2, Crustal structure of

365   the Krafla central volcano, *J. Geophys. Res.* **102**, no. B4, 7867–7886.

366 Campos, T., F. H. R. Bezerra, N. K. Srivastava, M. M. Vieira, and C. Vita-Finzi (2010). Holocene

367   tectonic uplift of the St Peter and St Paul Rocks (Equatorial Atlantic) consistent with

368   emplacement by extrusion, *Mar. Geol.* **271**, no. 1–2, 177–186, doi:

369   10.1016/j.margeo.2010.02.013.

370 Canales, J. P., J. A. Collins, and R. S. Detrick (2000). Seismic structure across the rift valley of

371   the Mid-Atlantic Ridge at 23°20' (MARK area): Implications for crustal accretion processes

372   at slow spreading ridges, *J. Geophys. Res.* **105**, no. B12, 28411–28425, doi:

373   10.1029/2000JB900301.

374 Christeson, G. L., J. A. Goff, and R. S. Reece (2019). Synthesis of Oceanic Crustal Structure

375   From Two-Dimensional Seismic Profiles, *Rev. Geophys.* **57**, doi: 10.1029/2019RG000641.

376 Chulick, G. S., S. Detweiler, and W. D. Mooney (2013). Seismic structure of the crust and

377   uppermost mantle of South America and surrounding oceanic basins, *J. South Am. Earth*

378   *Sci.* **42**, 260–276, doi: 10.1016/j.jsames.2012.06.002.

379 Chulick, G. S., and W. D. Mooney (2002). Seismic Structure of the Crust and Uppermost Mantle

380   of North America and Adjacent Oceanic Basins: A Synthesis, *Bull. Seismol. Soc. Am.* **92**,

381   no. 6, 2478–2492, doi: 10.1016/j.jsames.2012.06.002.

382 D'Eu, J. F., J. Y. Royer, and J. Perrot (2012). Long-term autonomous hydrophones for large-scale

383   hydroacoustic monitoring of the oceans, in *Proceedings of Oceans, 2012-Yeosu*, IEEE, 1–6,

384   doi: 10.1109/OCEANS-Yeosu.2012.6263519.

385 DeMets, C., R. G. Gordon, and D. F. Argus (2010). Geologically current plate motions, *Geophys.*

386   *J. Int.* **181**, 1–80, doi: 10.1111/j.1365-246X.2009.04491.x.

387   Dunn, R. A., V. Lekić, R. S. Detrick, and D. R. Toomey (2005). Three-dimensional seismic

388   structure of the Mid-Atlantic Ridge (35°N): Evidence for focused melt supply and lower

389   crustal dike injection, *J. Geophys. Res. Solid Earth* **110**, no. 9, 1–17, doi:

390   10.1029/2004JB003473.

391   Dziak, R. P., D. R. Bohnenstiehl, H. Matsumoto, C. G. Fox, D. K. Smith, M. Tolstoy, T. K. Lau,

392   J. H. Haxel, and M. J. Fowler (2004). P- and T-wave detection thresholds, Pn velocity

393   estimate, and detection of lower mantle and core P-waves on ocean sound-channel

394   hydrophones at the Mid-Atlantic Ridge, *Bull. Seism. Soc. Am.* **94**, no. 2, 665–677, doi:

395   10.1785/0120030156.

396   Dziak, R. P., C. G. Fox, H. Matsumoto, and A. E. Schreiner (1997). The April 1992 Cape

397   Mendocino earthquake sequence: Seismo-acoustic analysis utilizing fixed hydrophone

398   arrays, *Mar. Geophys. Res.* **19**, no. 2, 137–162, doi: 10.1023/A:1004256910362.

399   Dziewonski, A. M., and D. L. Anderson (1981). Preliminary reference Earth model, *Phys. Earth*

400   *Planet. Inter.* **25**, 297–356.

401   Ekström, G., M. Nettles, and A. M. Dziewoński (2012). The global CMT project 2004-2010:

402   Centroid-moment tensors for 13,017 earthquakes, *Phys. Earth Planet. Inter.* **200**–**201**, 1–9,

403   doi: 10.1016/j.pepi.2012.04.002.

404   Fox, C. G., H. Matsumoto, and T.-K. A. Lau (2001). Monitoring Pacific Ocean seismicity from

405   an autonomous hydrophone array, *J. Geophys. Res.* **106**, no. 10, 41834206, doi:

406   10.1029/2000JB900404.

407   Francis, T. J. G., I. T. Porter, and R. C. Lilwall (1978). Microearthquakes near the eastern end of

408   St Paul's fracture zone, *Geophys. J. R. Astron. Soc.* **53Reprint**, 201–217.

409   Gaherty, J. B., D. Lizarralde, J. A. Collins, G. Hirth, and S. Kim (2004). Mantle deformation

410   during slow seafloor spreading constrained by observations of seismic anisotropy in the

411   western Atlantic, *Earth Planet. Sci. Lett.* **228**, no. 3–4, 255–265, doi:

412   10.1016/j.epsl.2004.10.026.

413   Gasperini, L., G. Carrara Marco Ligi, P. Fabretti, D. Brunelli, A. Cipriani, S. Susini, and P.

414   Tartarotti (1997). New data on the geology of the Romanche FZ., equatorial Atlantic:

415   PRIMAR-96 cruise report, **3**, no. 59, 1–2.

416   Growe, K., I. Grevemeyer, S. Singh, and C. Papenberg (2019). Seismic structure of the St . Paul

417   Fracture Zone near 18°W in the Atlantic Ocean – evidence for a magmatic origin of crust,

418   *Geophys. Res. Abstr.* **21**, 4770.

419   Helffrich, G., J. Wookey, and I. Bastow (2013). *The Seismic Analysis Code: A Primer and User's*

420   *Guide*, Cambridge, UK.

421   Hooft, E. E. E., R. S. Detrick, D. R. Toomey, J. A. Collins, and J. Lin (2000). Crustal thickness

422   and structure along three contrasting spreading segments of the Mid-Atlantic Ridge, 33.5°-

423   35°N, *J. Geophys. Res. Solid Earth* **105**, no. B4, 8205–8226, doi: 10.1029/1999jb900442.

424   Kennett, B. L. N., and E. R. Engdahl (1991). Traveltimes for global earthquake location and

425   phase identification, *Geophys. J. Int.* **105**, no. 2, 429–465, doi: 10.1111/j.1365-

426   246X.1991.tb06724.x.

427   Lin, P. Y. P., J. B. Gaherty, G. Jin, J. A. Collins, D. Lizarralde, R. L. Evans, and G. Hirth (2016).

428   High-resolution seismic constraints on flow dynamics in the oceanic asthenosphere, *Nature*

429   **535**, no. 7613, 538–541, doi: 10.1038/nature18012.

430   Lin, J., and J. Phipps Morgan (1992). The spreading rate dependence of three-dimensional mid-

431   ocean ridge gravity structure, *Geophys. Res. Lett.* **19**, no. 1, 13–16.

432   Linehan, D. (1940). Earthquakes in the West Indian region, *Eos Trans. AGU* **21**, no. 2, 229–232,

433   doi: doi:10.1029/TR021i002p00229.

434   Lohman, R. B., and M. Simons (2005). Locations of selected small earthquakes in the Zagros

435   mountains, *Geochemistry, Geophys. Geosystems* **6**, no. 3, doi: 10.1029/2004GC000849.

436   Maia, M., I. Brehme, U. F. Fluminense, A. Briais, and D. Brunelli (2014). Preliminary report on

437   the COLMEIA Cruise, Equatorial Atlantic Recife, January 24 - Recife, February 28, 2013,

438   *InterRidge News* **22**, 52–56, doi: 10.1029/2005JB004210.Von.

439   Maia, M., S. Sichel, A. Briais, D. Brunelli, M. Ligi, N. Ferreira, T. Campos, B. Mougel, I.

440   Brehme, C. Hémond, *et al.* (2016). Extreme mantle uplift and exhumation along a

441   transpressive transform fault, *Nat. Geosci.* **9**, no. 8, 619–623, doi: 10.1038/ngeo2759.

442   Mark, H. F., D. Lizarralde, J. A. Collins, N. C. Miller, G. Hirth, J. B. Gaherty, and R. L. Evans

443   (2019). Azimuthal Seismic Anisotropy of 70-Ma Pacific-Plate Upper Mantle, *J. Geophys.*

444   *Res. Solid Earth* **124**, no. 2, 1889–1909, doi: 10.1029/2018JB016451.

445   de Melo, G., and A. F. do Nascimento (2018). Earthquake Magnitude Relationships for the Saint

446   Peter and Saint Paul Archipelago, Equatorial Atlantic, *Pure Appl. Geophys.* **175**, no. 3, 741–

447   756, doi: 10.1007/s00024-017-1732-6.

448   Müller, R. D., M. Sdrolias, C. Gaina, and W. R. Roest (2008). Age, spreading rates, and

449   spreading asymmetry of the world's ocean crust, *Geochem. Geophys. Geosyst* **9**, no. 4, 1–

450   19, doi: 10.1029/2007GC001743.

451   Nicolas, A., and N. I. Christensen (2011). Formation of anisotropy in upper mantle peridotites - A

452   review, in *Composition, structure and dynamics of the lithosphere-asthenosphere system,*

453   *Geodynamics* K. Fuchs, and C. Froidevaux(Editors), American Geophysical Union,

454   Washington, D. C., 111–123, doi: 10.1029/gd016p0111.

455   Le Pichon, X., R. E. Houtz, C. L. Drake, and J. E. Nafe (1965). Crustal structure of the mid-

456   ocean ridges: 1. Seismic refraction measurements, *J. Geophys. Res.* **70**, no. 2, 319–339, doi:

457   10.1029/jz070i002p00319.

458   Raitt, R. W., J. Shor, G. G., T. J. G. Francis, and G. B. Morris (1969). Anisotropy of the Pacific

459   upper mantle, *J. Geophys. Res.* **74**, no. 12, 3095–3109, doi:

460   https://doi.org/10.1029/JB074i012p03095.

461   Ribe, N. M. (1989). Seismic anisotropy and mantle flow, *J. Geophys. Res.* **94**, no. B4, 4213–

462   4223, doi: 10.1029/JB094iB04p04213.

463   Schaeffer, A. J., and S. Lebedev (2013). Global shear speed structure of the upper mantle and

464   transition zone, *Geophys. J. Int.* **194**, no. 1, 417–449, doi: 10.1093/gji/ggt095.

465   Slack, P., C. G. Fox, and R. P. Dziak (1999). P wave detection thresholds, Pn velocity estimates,

466   and T wave location uncertainty from oceanic hydrophones, *J. Geophys. Res.* **104**, 61–72.

467   Sleep, N. H. (1975). Formation of Oceanic Crust: Some Thermal Constraints, *J. Geophys. Res.*

468   **80**, no. 29, 4037–4042.

469   Smith, D. K., R. P. Dziak, C. Palmiotto, R. Parnell-Turner, and A. Zheleznov (2012). The

470   seismicity of the equatorial Mid-Atlantic Ridge and its long-offset transforms, *Abstract*

471   *OS13B-1720 Presented at 2012 Fall Meeting AGU, San Francisco. Calif. 5-9 Dec*.

472   Sohn, R. A., and J. A. Hildebrand (2001). Hydroacoustic earthquake detection in the Arctic Basin

473   with the Spinnaker array, *Bull. Seismol. Soc. Am.* **91**, no. 3, 572–579, doi:

474   10.1785/0120000099.

475   Sokos, E. N., and J. Zahradnik (2008). ISOLA: a Fortran code and a Matlab GUI to perform

476   multiple-point source inversion of seismic data, *Comput. Geosci.* **34**, no. 8, 967–977, doi:

477   10.1016/j.cageo.2007.07.005.

478   Taylor, J. (1997). *Introduction to Error Analysis, the Study of Uncertainties in Physical*

479   *Measurements*, University Science Books, New York, NY.

480   Turcotte, D. L., and G. Schubert (2002). *Geodynamics*, Cambridge University Press, doi:

481   10.1017/CBO9780511807442.

482   Udintsev, G. B., H. J., V. G. Udintsev, and A. B. Knjazev (1996). Topography of the Equatorial

483   Segment of the Mid-Atlantic Ridge After Multi-Beam Echo-sounding., in *Equatorial*

484   *Segment of the Mid-Atlantic Ridge: IOC Technical Series No. 46* G. B. Udintsev(Editor),

485   United Nations Educational, Scientific and Cultural Organization, Paris, France, 8–15.

486   VanderBeek, B. P., and D. R. Toomey (2017). Shallow Mantle Anisotropy Beneath the Juan de

487   Fuca Plate, *Geophys. Res. Lett.* **44**, no. 22, 11,382-11,389, doi: 10.1002/2017GL074769.

488   Walker, D. A., C. S. McCreery, and G. H. Sutton (1983). Spectral characteristics of high-

489   frequency PN, SN phases in the western Pacific, *J. Geophys. Res.* **88**, no. B5, 4289–4298.

490   Wessel, P., W. H. F. Smith, R. Scharoo, J. Luis, and F. Wobbe (2013). Generic Mapping Tools:

491   Improved Version Released, *Eos Trans. AGU* **94**, no. 45, 409–410.

492   Weston, J., A. M. G. Ferreira, and G. J. Funning (2012). Systematic comparisons of earthquake

493   source models determined using InSAR and seismic data, *Tectonophysics* **532**–**535**, 61–81,

494   doi: 10.1016/j.tecto.2012.02.001.

495   Zhang, Z., and S. Karato (1995). Lattice preferred orientation of olivine aggregates in simple

496   shear, *Nature* **375**, 774–777.

497

498

499

500   **Author mailing addresses**

501   Departamento de Geofísica, Federal University of Rio Grande do Norte, Natal, Brazil

502   (GWSM, AFN)

503   Institute of Geophysics and Planetary Physics, Scripps Institution of Oceanography, University of

504   California, San Diego, CA, USA

505   (RPT)

506   NOAA, Pacific Marine Environmental Laboratory, Newport, OR, USA

507   (RPD)

508

509   National Science Foundation, Alexandria, VA, USA

510   (DKS)

511

512   Laboratoire Geosciences Ocean, CNRS and University of Brest

513   LGO-IUEM, rue Dumont Durville, 29280 Plouzane, France

514   (MM and JYR)

515

516

517

518   **Figures**
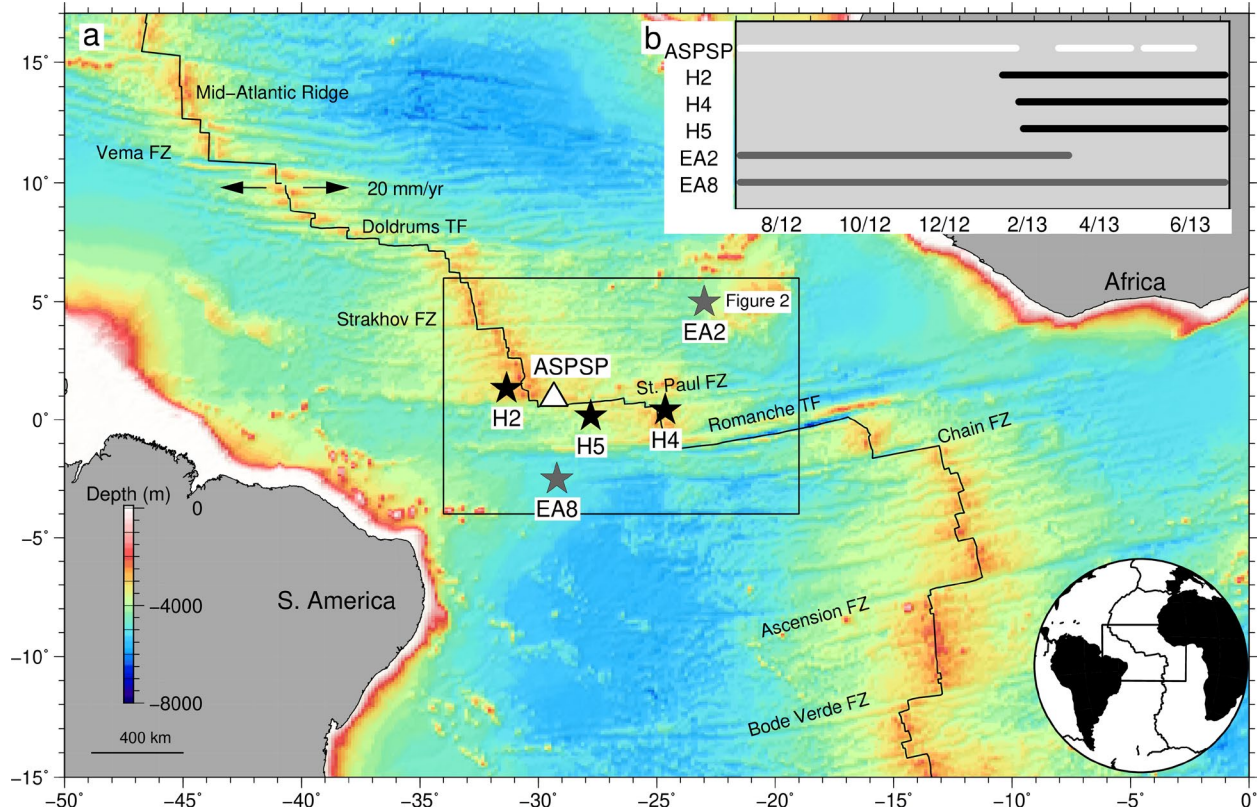
521   **Figure 1. a)** Regional bathymetric map of equatorial Atlantic ocean. White triangle shows

522   ASPSP seismograph station, located on St. Peter and St. Paul islets; black/gray stars are

523   COLMEIA / EA hydrophone networks, respectively (Smith *et al.*, 2012; Maia *et al.*, 2014); black

524   line is Mid-Atlantic Ridge, with selected transforms and half-spreading rate noted (arrows).

525   Black box shows location of Figure 2. **b)** Bars show operation intervals of instruments for each

526   network: ASPSP (white); COLMEIA (black) and EA (gray).
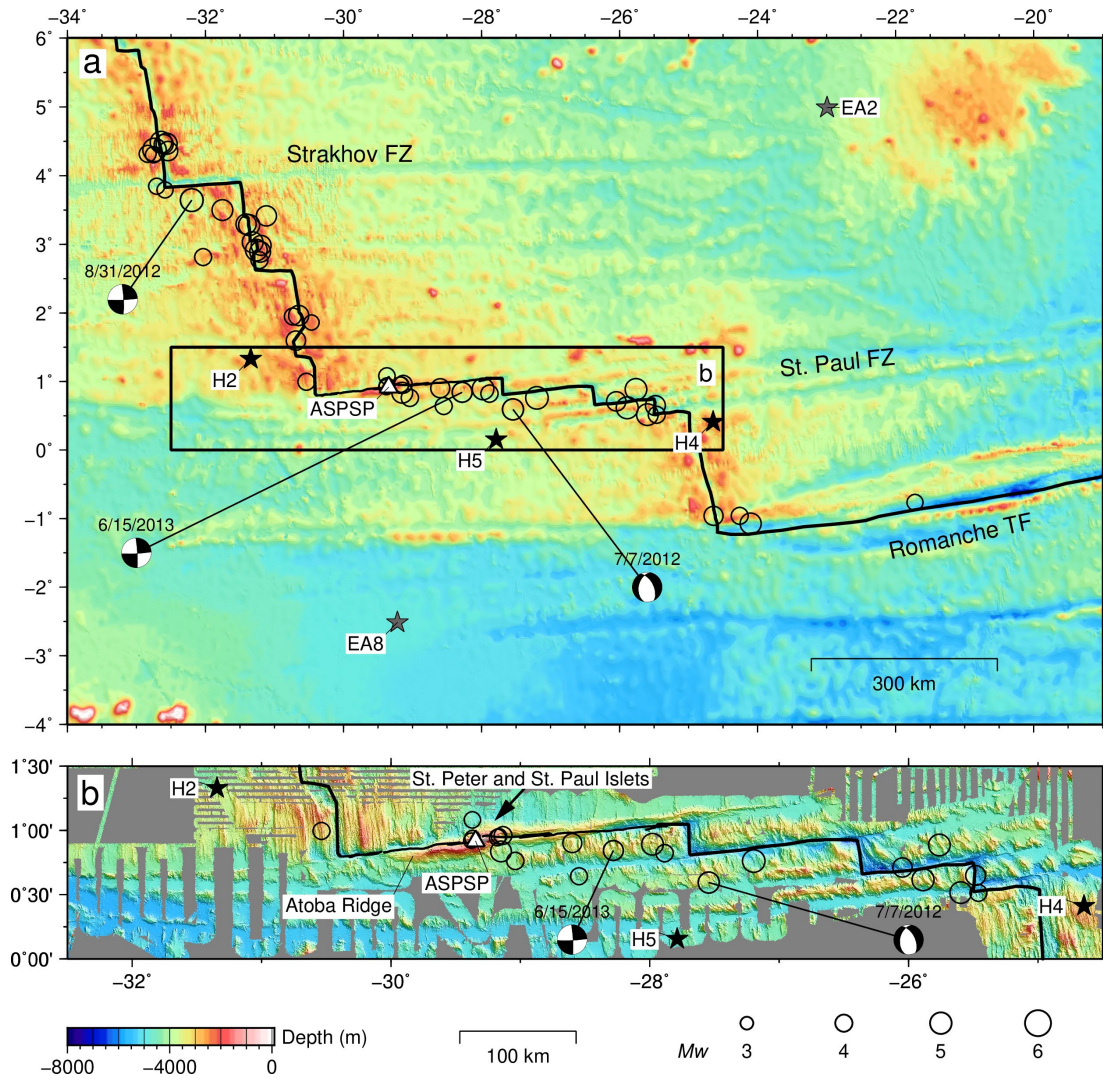
Figure 2. a) Bathymetric map of equatorial Atlantic ocean. Black box shows location of (b).

Circles are earthquakes used in *Pn* analysis, scaled by M_W; triangle shows ASPSP

station; black/gray stars are COLMEIA / EA hydrophone networks, respectively (Maia *et al.*,

2013; Smith *et al.,* 2012); black line is Mid-Atlantic Ridge, with selected transforms labeled;

beach-balls are centroid moment tensors for three exemplar earthquakes (Ekström *et al.*, 2012),

waveforms shown in Figures 4 and 5. **b)** Bathymetric map showing details of St Peter and St Paul

fracture zone (from Udintsev *et al.*, 1996; Gasperini *et al.*, 1997; Maia *et al.*, 2016).
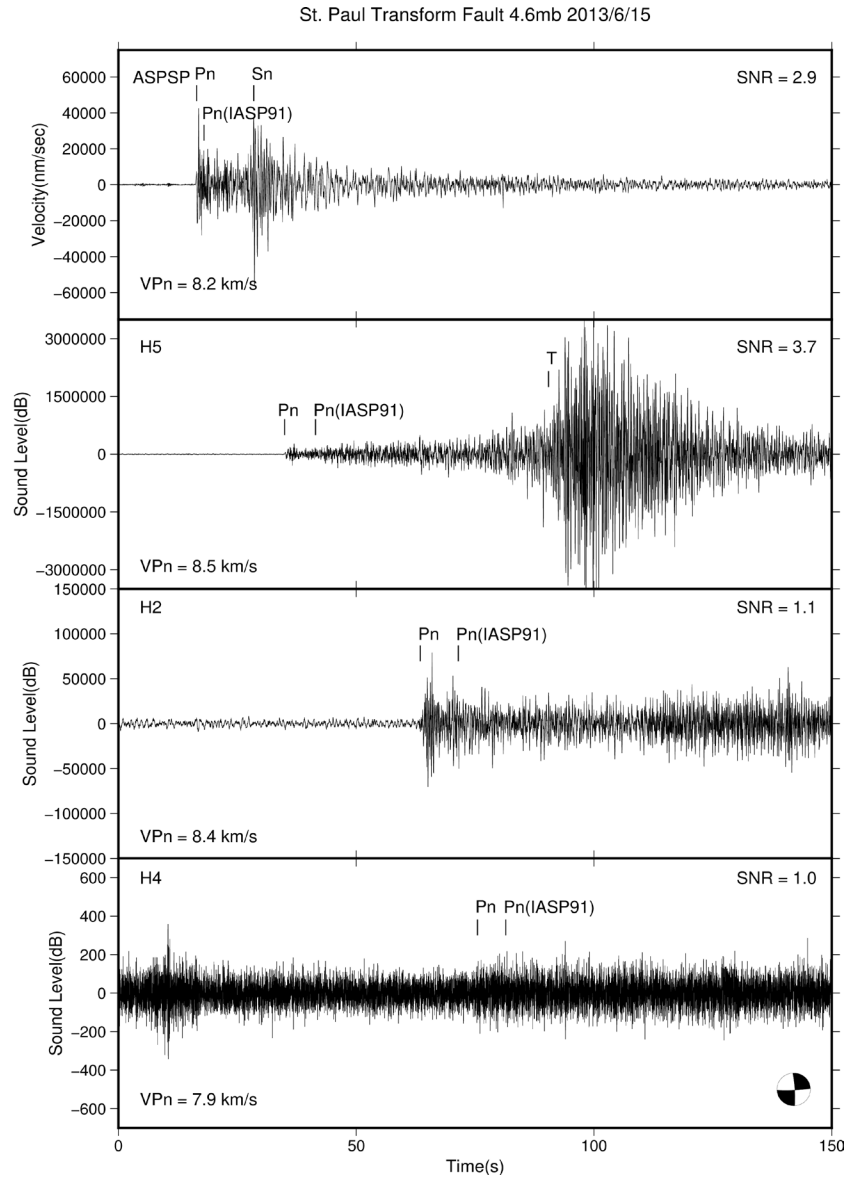
553

554
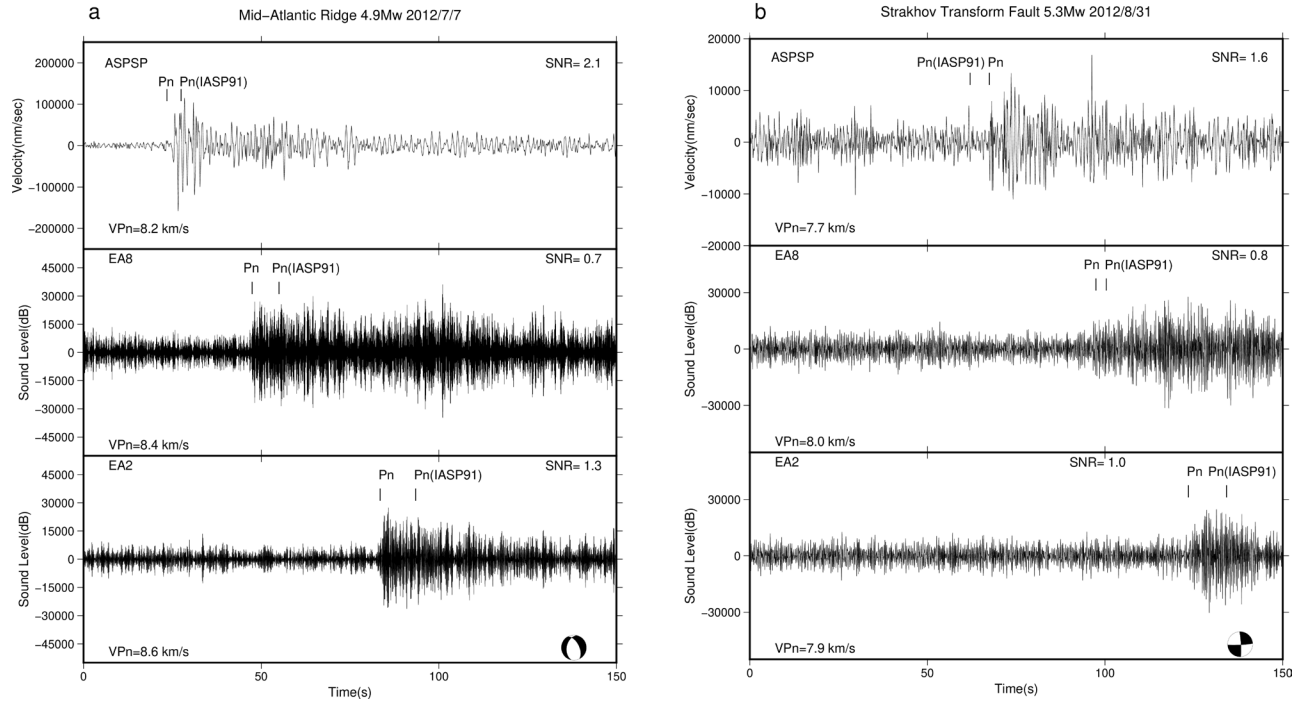
555　**Figure 3.** Example waveforms recorded by the ASPSP seismograph and EA array hydrophones,

556　with 4–12 Hz and 6–20 Hz Butterworth filter applied, respectively. **a)** M_w 4.9 normal faulting

557　event on 7th July 2012, located on the St Paul transform fault at 27.5°W. Picked *Pn* arrivals, and

558　*Pn* arrivals predicted by IASP91 model are marked; beach-balls are centroid moment tensors

559　(Ekström et al., 2012); V_{Pn} and signal to noise ratio (SNR) noted for each station (this study),

560　SNR calculated in a window 1.5 s either side of *Pn* arrival. **b)** M_w 5.3 strike-slip event on 31st

561　August 2012, located on Strakhov transform fault near 32.5°W.

562

563

564 **Figure 4.** Example of waveforms recorded by the ASPSP seismograph and COLMEIA

565 hydrophones, with 4–12 Hz and 6–20 Hz Butterworth filter applied, respectively, for mb 4.6 strike-

566 slip event on 15th June 2013, located near St Paul transform fault at 29.5°W. Picked *Pn* arrivals,

567 and *Pn* arrivals predicted by IASP91 model are marked; beach-balls are centroid moment tensors

568 (Ekström et al., 2012); V_{Pn} and SNR noted for each station (this study).

569

570

571
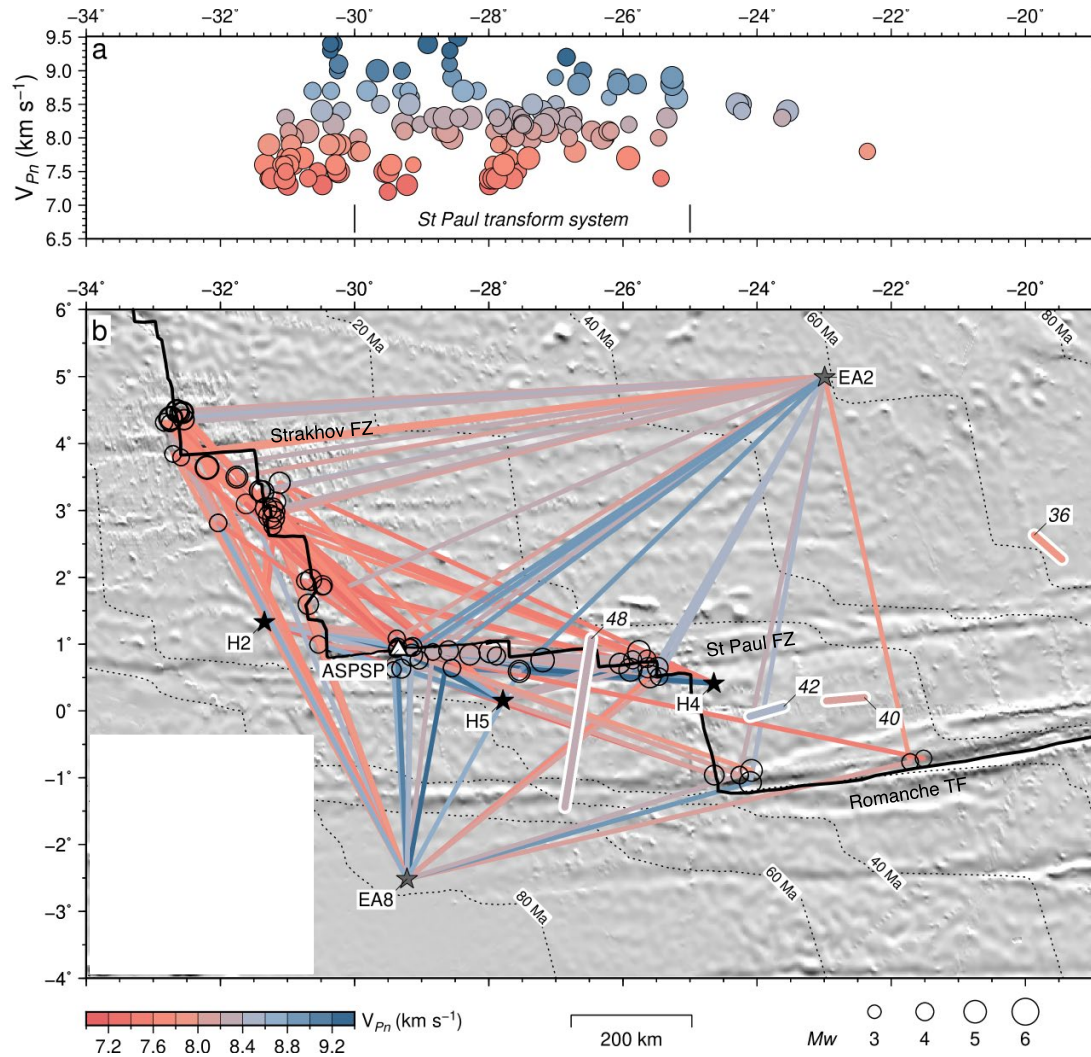
572 **Figure 5. a)** V$_{Pn}$ plotted against mean longitude of ray path. Circle radius scaled by magnitude

573 of source event; colored by V$_{Pn}$; St Paul transform system marked by vertical bars. **b)** Shaded

574 relief map showing stations, earthquakes, and ray paths. Circles are earthquakes used in *Pn*

575 analysis, scaled by M$_W$; thin colored lines are ray paths shaded with *Pn* velocity; white triangle

576 is ASPSP station; black/gray stars are COLMEIA / EA hydrophone networks, respectively (Maia

577 *et al.,* 2013; Smith *et al.,* 2012); thick lines numbered 48, 42, 40, and 36 are seismic refraction

578 profiles from cruise AT40-180 (Le Pichon *et al.*, 1965), shaded by velocity; dotted lines are

579 isochrons

580   , modified from Müller *et al.* (2008) to remove artifacts associated with fracture zone traces. **c)**

581   Histogram of difference between velocity estimates from refraction experiment (Le Pichon *et al.,*

582   1965), and intersecting ray paths from this study; positive values indicate faster velocities

583   estimated by refraction experiment; dark/light gray bars are velocities from profiles 48 and 42,
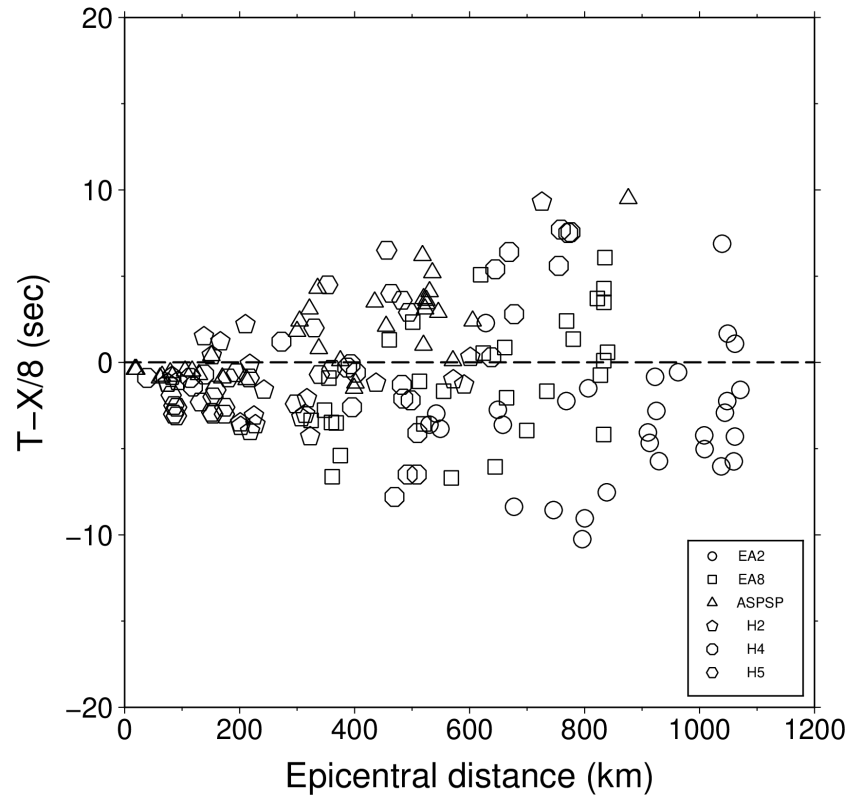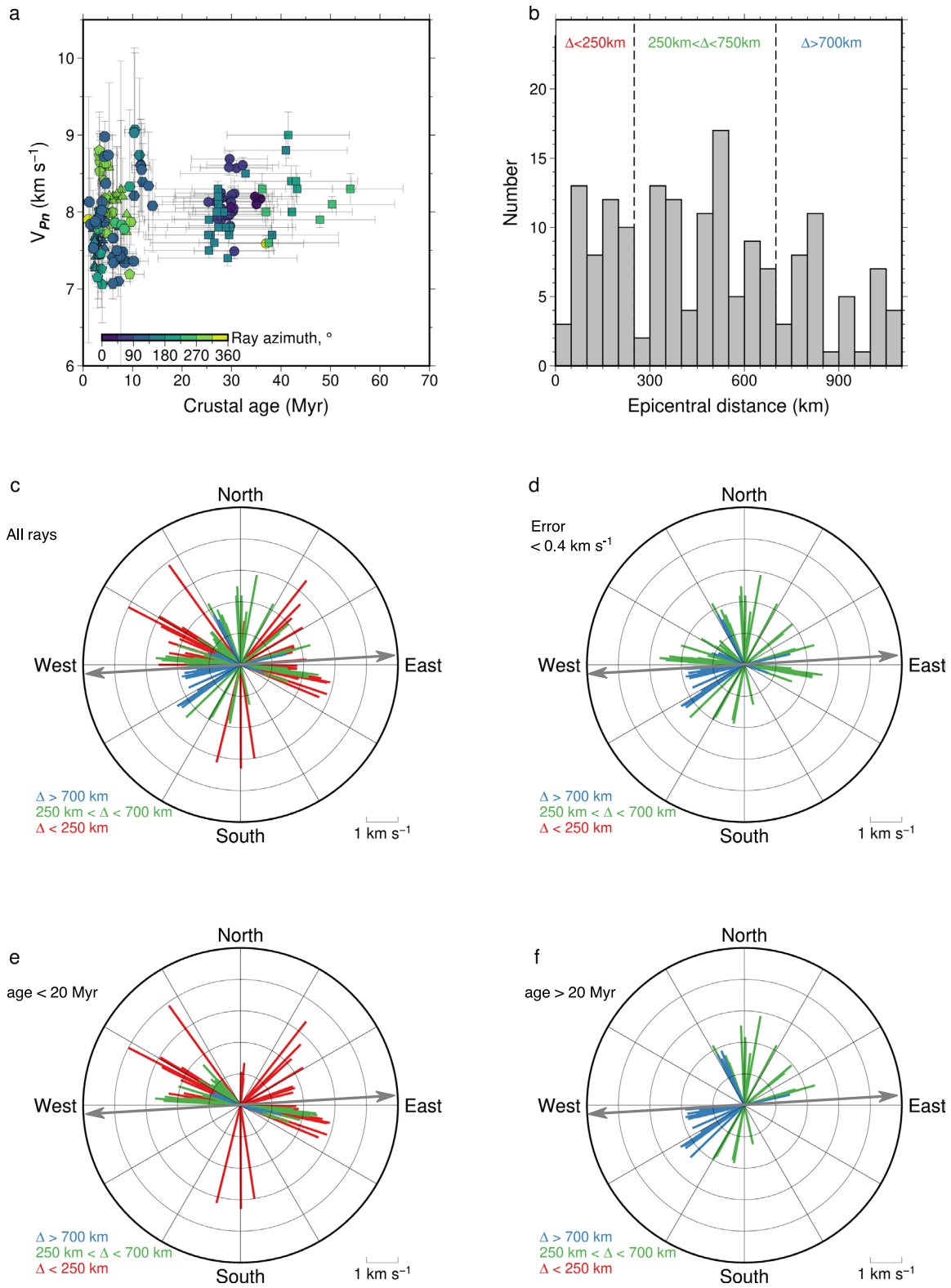
584   respectively.

585

586

587

588

589

590

Figure 6. Reduced travel time versus epicentral distance for the 152 ray paths, plotted with a reduction velocity of 8 km s^{-1}, approximately corresponding to velocity immediately Moho from PREM and IASP91 models (dotted line; Dziewonski and Anderson, 1981; Kennett and Engdahl, 1991); key shows recording station symbols.

597   **Figure 7. a)** V_{Pn} plotted against oceanic crustal age at epicental location (crustal ages assigned

598   from model of Müller *et al.* (2008), colored by ray azimuth. Triangles are estimates from ASPSP

599   station; black/gray symbols are from COLMEIA / EA hydrophone stations, respectively (see key

600   in Figure 6); horizontal error bars are 2σ crustal age along ray path, vertical error bars from

601   uncertainty described in text. **b)** Histogram of epicentral distances; dotted lines show cut-offs used

602   to define categories in anisotropy analysis. **c)** Rose diagram showing V_{Pn} vs. azimuth for all rays;

603   length of lines scaled by $V_{Pn,}$ colored by epicentral distance; gray arrows show plate spreading

604   azimuth. **d)** V_{Pn} vs. azimuth for rays with uncertainty < 0.4 km s^{-1}, colored by epicentral distance.

605   **e)** V_{Pn} vs. azimuth for rays sampling crust < 20 Myr in age, colored by epicentral distance. **f)** V_{Pn}

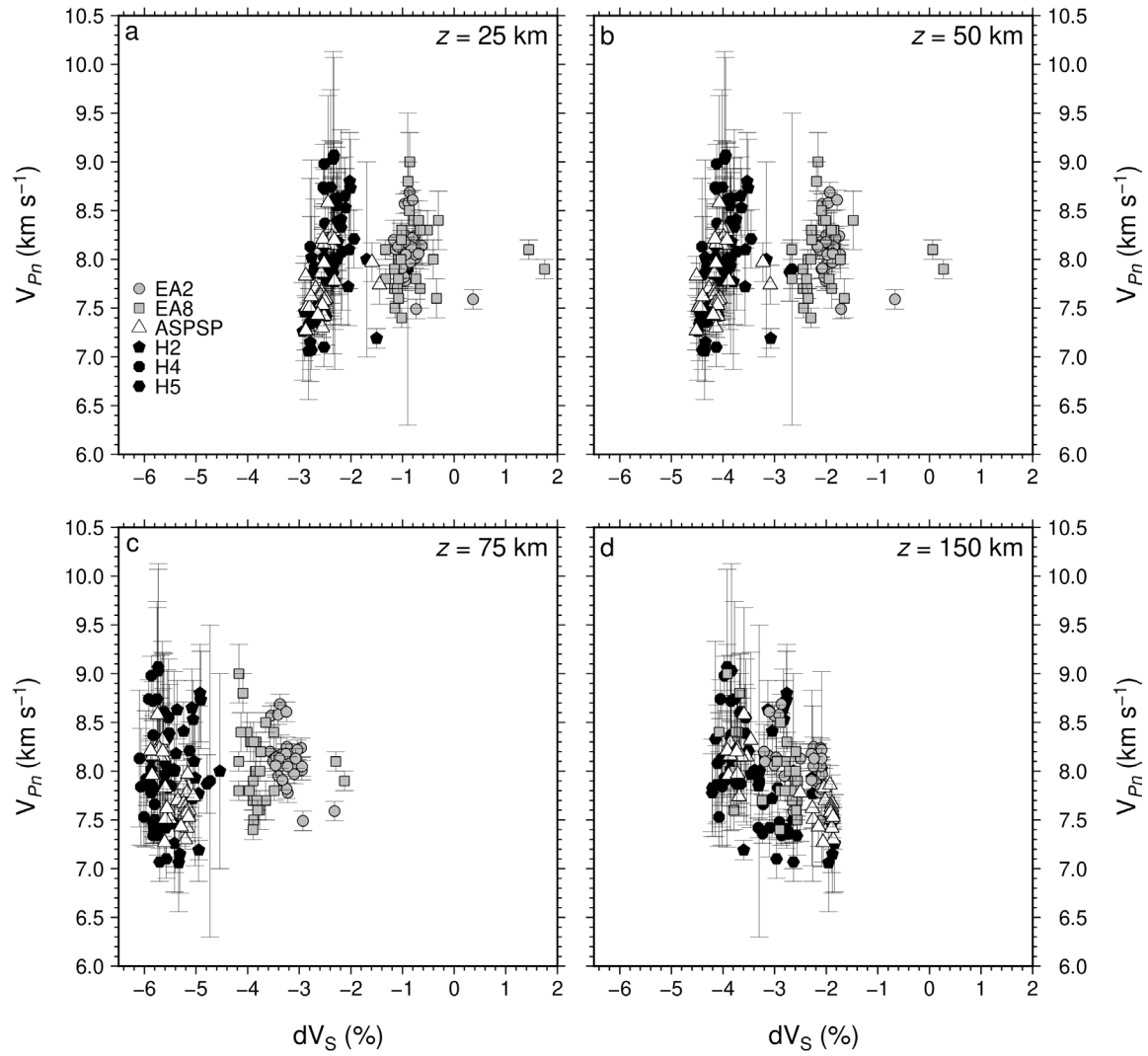606   vs. azimuth for rays sampling crust > 20 Myr in age, colored by epicentral distance.

607

608
609
610
611
612
613
614
615
616
617
618
619
620
621
622

623 **Figure 8 (a-d)** Relationship between V_{Pn} and vertically polarized tomographic shear velocity

624 anomaly at depths of 25, 50, 75 and 150 km, respectively from global model SL2013sv (Schaeffer

625 and Lebedev, 2013). Triangles are estimates from ASPSP station; black/gray symbols are from

626 COLMEIA / EA hydrophone stations, respectively (see key).

627

Station name	Sensor type	Lat, °N	Lon, °E	Depth bsl, m	Cable length, m	Water delay, s	Crust path correction, s	Crust travel time correction, s
ASPSP	S	0.9169	-29.3459	-16	-	-	12.5	1.9
EA2	H	4.9907	-22.9931	800	3912	2.10	23.8	7.2
EA8	H	-2.5159	-29.2181	800	3242	2.54	23.0	6.5
H2	H	1.3297	-31.3445	700	2260	1.57	21.8	5.5
H4	H	0.4123	-24.6437	700	1860	1.24	21.3	5
H5	H	0.1552	-27.7875	700	3060	2.04	22.8	6.3

628

629

630   **Table 1.** Details of seismograph (S) and hydrophone (H) sensors used for *Pn* analysis in this

631   study; including depth below sea level (bsl), cable length, and water/crust corrections.

632